

Deep exclusive π^+ electroproduction off the proton at CLAS

K. Park,³⁵ R.W. Gothe,³⁴ M. Guidal,²¹ J.M. Laget,³⁵ K.P. Adhikari,²⁹ M. Aghasyan,¹⁸ M.J. Amarian,²⁹ M. Anghinolfi,¹⁹ H. Avakian,³⁵ H. Bagdasaryan,^{39,41} J. Ball,⁷ N.A. Baltzell,¹ M. Battaglieri,¹⁹ I. Bedlinsky,²² R. P. Bennett,²⁹ A. S. Biselli,^{11,30} C. Bookwalter,¹³ S. Boiarinov,³⁵ W.J. Briscoe,¹⁵ W.K. Brooks,^{36,35} V.D. Burkert,³⁵ D.S. Carman,³⁵ A. Celentano,¹⁹ S. Chandavar,²⁸ G. Charles,⁷ M. Contalbrigo,¹⁷ V. Crede,¹³ A. D'Angelo,^{20,32} A. Daniel,²⁸ N. Dashyan,⁴¹ R. De Vita,¹⁹ E. De Sanctis,¹⁸ A. Deur,³⁵ C. Djalali,³⁴ G.E. Dodge,²⁹ D. Doughty,^{8,35} R. Dupre,⁷ H. Egiyan,³⁵ A. El Alaoui,¹ L. El Fassi,¹ P. Eugenio,¹³ G. Fedotov,³⁴ S. Fegan,³⁷ J.A. Fleming,¹⁰ T.A. Forest,¹⁶ M. Garçon,⁷ N. Gevorgyan,⁴¹ G.P. Gilfoyle,³¹ K.L. Giovanetti,²³ F.X. Girod,³⁵ W. Gohn,⁹ E. Golovatch,³³ L. Graham,³⁴ K.A. Griffioen,⁴⁰ B. Guegan,²¹ L. Guo,^{12,35} K. Hafidi,¹ H. Hakobyan,^{36,41} C. Hanretty,³⁹ D. Heddle,^{8,35} K. Hicks,²⁸ D. Ho,⁵ M. Holtrop,²⁶ Y. Ilieva,^{34,15} D.G. Ireland,³⁷ B.S. Ishkhanov,³³ D. Jenkins,³⁸ H.S. Jo,²¹ D. Keller,³⁹ M. Khandaker,²⁷ P. Khetarpal,¹² A. Kim,²⁴ W. Kim,²⁴ F.J. Klein,⁶ S. Koirala,²⁹ A. Kubarovsky,^{30,33} V. Kubarovsky,³⁵ S.E. Kuhn,²⁹ S.V. Kuleshov,^{36,22} K. Livingston,³⁷ H.Y. Lu,⁵ I. J.D. MacGregor,³⁷ Y. Mao,³⁴ N. Markov,⁹ D. Martinez,¹⁶ M. Mayer,²⁹ B. McKinnon,³⁷ C.A. Meyer,⁵ T. Mineeva,⁹ M. Mirazita,¹⁸ V. Mokeev,^{35,33,*} H. Moutarde,⁷ E. Munevar,³⁵ C. Munoz Camacho,²¹ P. Nadel-Turonski,³⁵ C.S. Nepali,²⁹ S. Niccolai,^{21,15} G. Niculescu,^{23,28} I. Niculescu,^{23,35} M. Osipenko,¹⁹ A.I. Ostrovidov,¹³ L.L. Pappalardo,¹⁷ R. Paremuzyan,^{41,†} S. Park,¹³ E. Pasyuk,^{35,2} S. Anefalos Pereira,¹⁸ E. Phelps,³⁴ S. Pisano,¹⁸ O. Pogorelko,²² S. Pozdniakov,²² J.W. Price,³ S. Procureur,⁷ D. Protopopescu,^{37,26} A.J.R. Puckett,³⁵ B.A. Raue,^{12,35} G. Ricco,^{14,‡} D. Rimal,¹² M. Ripani,¹⁹ G. Rosner,³⁷ P. Rossi,¹⁸ F. Sabatié,⁷ M.S. Saini,¹³ C. Salgado,²⁷ D. Schott,¹² R.A. Schumacher,⁵ E. Seder,⁹ H. Seraydaryan,²⁹ Y.G. Sharabian,³⁵ E.S. Smith,³⁵ G.D. Smith,³⁷ D.I. Sober,⁶ D. Sokhan,²¹ S.S. Stepanyan,²⁴ P. Stoler,³⁰ I.I. Strakovsky,¹⁵ S. Strauch,^{34,15} M. Taiuti,^{14,‡} W. Tang,²⁸ C.E. Taylor,¹⁶ Ye Tian,³⁴ S. Tkachenko,³⁹ A. Trivedi,³⁴ M. Ungaro,^{35,30} B. Vernarsky,⁵ H. Voskanyan,⁴¹ E. Voutier,²⁵ N.K. Walford,⁶ D.P. Watts,¹⁰ L.B. Weinstein,²⁹ D.P. Weygand,³⁵ M.H. Wood,^{4,34} N. Zachariou,³⁴ J. Zhang,^{35,29} Z.W. Zhao,³⁹ and I. Zonta^{20,§}

(The CLAS Collaboration)

¹Argonne National Laboratory, Argonne, Illinois 60439, USA

²Arizona State University, Tempe, Arizona 85287-1504, USA

³California State University, Dominguez Hills, Carson, California 90747, USA

⁴Canisius College, Buffalo, New York 14208, USA

⁵Carnegie Mellon University, Pittsburgh, Pennsylvania 15213, USA

⁶Catholic University of America, Washington, D.C. 20064, USA

⁷CEA, Centre de Saclay, Irfu/Service de Physique Nucléaire, 91191 Gif-sur-Yvette, France

⁸Christopher Newport University, Newport News, Virginia 23606, USA

⁹University of Connecticut, Storrs, Connecticut 06269, USA

¹⁰Edinburgh University, Edinburgh EH9 3JZ, United Kingdom

¹¹Fairfield University, Fairfield Connecticut 06824, USA

¹²Florida International University, Miami, Florida 33199, USA

¹³Florida State University, Tallahassee, Florida 32306, USA

¹⁴Università di Genova, 16146 Genova, Italy

¹⁵The George Washington University, Washington, D.C. 20052, USA

¹⁶Idaho State University, Pocatello, Idaho 83209, USA

¹⁷INFN, Sezione di Ferrara, 44100 Ferrara, Italy

¹⁸INFN, Laboratori Nazionali di Frascati, 00044 Frascati, Italy

¹⁹INFN, Sezione di Genova, 16146 Genova, Italy

²⁰INFN, Sezione di Roma Tor Vergata, 00133 Rome, Italy

²¹Institut de Physique Nucléaire ORSAY, Orsay, France

²²Institute of Theoretical and Experimental Physics, Moscow, 117259, Russia

²³James Madison University, Harrisonburg, Virginia 22807, USA

²⁴Kyungpook National University, Daegu 702-701, Republic of Korea

²⁵LPSC, Université Joseph Fourier, CNRS/IN2P3, INPG, Grenoble, France

²⁶University of New Hampshire, Durham, New Hampshire 03824-3568, USA

²⁷Norfolk State University, Norfolk, Virginia 23504, USA

²⁸Ohio University, Athens, Ohio 45701, USA

²⁹Old Dominion University, Norfolk, Virginia 23529, USA

³⁰Rensselaer Polytechnic Institute, Troy, New York 12180-3590, USA

³¹University of Richmond, Richmond, Virginia 23173, USA

³²*Universita' di Roma Tor Vergata, 00133 Rome, Italy*

³³*Skobeltsyn Nuclear Physics Institute, Skobeltsyn Nuclear Physics Institute, 119899 Moscow, Russia*

³⁴*University of South Carolina, Columbia, South Carolina 29208, USA*

³⁵*Thomas Jefferson National Accelerator Facility, Newport News, Virginia 23606, USA*

³⁶*Universidad Técnica Federico Santa María, Casilla 110-V Valparaíso, Chile*

³⁷*University of Glasgow, Glasgow G12 8QQ, United Kingdom*

³⁸*Virginia Polytechnic Institute and State University, Blacksburg, Virginia 24061-0435, USA*

³⁹*University of Virginia, Charlottesville, Virginia 22901, USA*

⁴⁰*College of William and Mary, Williamsburg, Virginia 23187-8795, USA*

⁴¹*Yerevan Physics Institute, 375036 Yerevan, Armenia*

(Dated: March 19, 2019)

The exclusive electroproduction of π^+ above the resonance region was studied using the CEBAF Large Acceptance Spectrometer (CLAS) at Jefferson Laboratory by scattering a 6-GeV continuous electron beam off a hydrogen target. The large acceptance and good resolution of CLAS, together with the high luminosity, allowed us to measure the cross section for the $\gamma^*p \rightarrow n\pi^+$ process in 140 (Q^2 , x_B , t) bins: $0.16 < x_B < 0.58$, $1.6 \text{ GeV}^2 < Q^2 < 4.5 \text{ GeV}^2$ and $0.1 \text{ GeV}^2 < -t < 5.3 \text{ GeV}^2$. For most bins, the statistical accuracy is on the order of a few percent. Differential cross sections are compared to two theoretical models, based either on hadronic (Regge phenomenology) or on partonic (handbag diagram) degrees of freedom. Both can describe the gross features of the data reasonably well, but differ strongly in their ingredients. If the handbag approach can be validated in this kinematical region, our data contain the interesting potential to experimentally access transversity Generalized Parton Distributions.

PACS numbers: 13.60.Hb, 25.30.Rw

I. INTRODUCTION

One of the major challenges in contemporary nuclear physics is the study of the transition between hadronic and partonic pictures of the strong interaction. At asymptotically short distances, the strong force is actually weak and the appropriate degrees of freedom are the quarks and gluons (partons) whose interaction can be quantified very precisely by perturbative Quantum Chromodynamics (pQCD). However, at larger distances on the order of one Fermi, effective theories that take hadrons as elementary particles whose interactions are described by the exchange of mesons appear more applicable. The connection between these two domains is not well understood. In order to make progress, a systematic study of a series of hadronic reactions probing these intermediate distance scales is necessary. The exclusive electroproduction of a meson (or of a photon) from a nucleon, $\gamma^*N \rightarrow N'M$, is particularly interesting. Indeed, it offers two ways to vary the scale of the interaction and therefore to study this transition regime. One can vary the virtuality of the incoming photon $Q^2 = -(e - e')^2$, which

effectively represents the transverse size of the probe, or the momentum transfer to the nucleon $t = (N - N')^2$, which effectively represents the transverse size of the target. Here, e and e' are the initial and scattered electron four-momenta and N and N' are the initial and final nucleon four-momenta, respectively. Figure 1 sketches the transition regions that have been experimentally explored up to now (lightly shaded areas) as a function of these two variables, Q^2 and $|t|$. In photoproduction, keeping only $|t| > 3 \text{ GeV}^2$ data, the relevant experiments are from SLAC [1] and JLab [2]. In electroproduction, keeping only $Q^2 > 1.5 \text{ GeV}^2$ data, the relevant experiments are from Cornell [3, 4], JLab [5] and HERMES [6]. In these latter electroproduction experiments, the phase space was divided into only a few bins in Q^2 , x_B or W , and t . The darkly shaded area in Fig. 1 represent the phase space covered by the present work. It is divided into 140 (Q^2 , x_B or W , t) bins.

We also display in Fig. 1 the asymptotically large- Q^2 or large- $|t|$ partonic diagrams, as well as the low- Q^2 and low- $|t|$ hadronic diagram, of the $\gamma^*N \rightarrow N'M$ process. At asymptotically large Q^2 and small $|t|$ (along the vertical axis in Fig. 1), the exclusive electroproduction of a meson should be dominated by the so-called “handbag diagram” [7–10]. The initial virtual photon hits a quark in the nucleon and this same quark, after a single gluon exchange, ends up in the final meson. A QCD factorization theorem [10] states that the complex quark and gluon non-perturbative structure of the nucleon is described by the Generalized Parton Distributions (GPDs). For the π^+ channel at leading twist in QCD, i.e. at asymptoti-

*Current address:Skobeltsyn Nuclear Physics Institute, 119899 Moscow, Russia

†Current address:Institut de Physique Nucléaire ORSAY, Orsay, France

‡Current address:INFN, Sezione di Genova, 16146 Genova, Italy

§Current address:Universita' di Roma Tor Vergata, 00133 Rome Italy

cally large Q^2 , the longitudinal part of the cross section σ_L is predicted to be dominant over the transverse part σ_T . Precisely, $d\sigma_L/dt$ should scale as $1/Q^6$ at fixed x_B and $|t|$, while $d\sigma_T/dt$ should scale as $1/Q^8$. It is predicted that σ_L is sensitive to the helicity-dependent GPDs \tilde{E} and \tilde{H} [10] while, if higher-twist effects are taken into account, σ_T is sensitive to the transversity GPDs, H_T and $\tilde{E}_T = 2\tilde{H}_T + E_T$ [11].

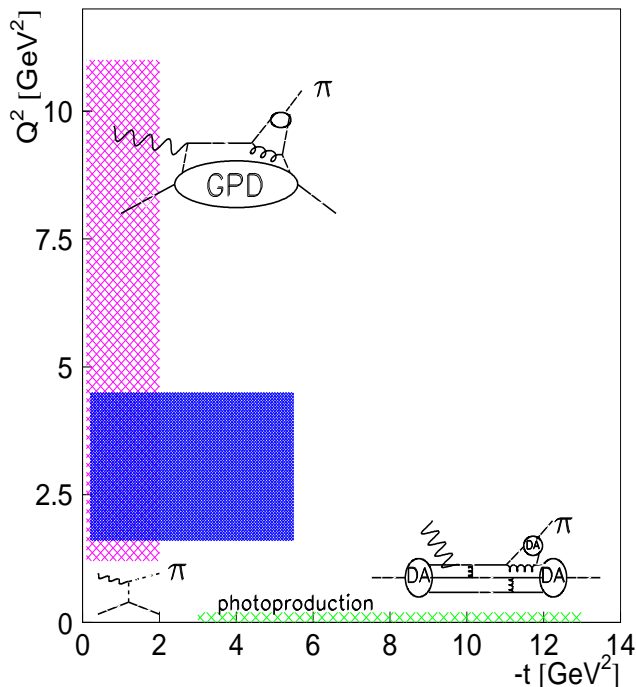


FIG. 1: (color online). Schematic representation of the $\gamma^* N \rightarrow N' \pi$ process (above the resonance region) in different regions of the (Q^2, t) plane. The Feynman diagrams describe the reaction in terms of meson exchanges at low Q^2 and $|t|$, in terms of GPDs at large Q^2 and small $|t|$, and in terms of hadron distribution amplitudes (DA) at large $|t|$. The lightly shaded areas (magenta and green online) represent approximately the experimentally explored regions up to now. The darkly shaded area (blue online) represents the phase space covered by this work.

At large values of $|t|$, in photoproduction (i.e. along the horizontal axis in Fig. 1) but also presumably in electroproduction, the $\gamma^{(*)} N \rightarrow N' M$ process should be dominated by the coupling of the virtual photon to one of the valence quarks of the nucleon (or of the produced meson), with minimal interactions among the valence quarks. In this regime, a QCD factorization theorem states that the complex structure of the hadrons is described by distribution amplitudes (DA) which at small distances (large $|t|$) can be reduced to the lowest Fock states, i.e. 3 quarks for the nucleon and $q\bar{q}$ for the meson [12]. At sufficiently high energy, constituent counting rules (CCR) [13] pre-

dict an s^{-7} scaling of the differential cross section $d\sigma/dt$ at fixed center-of-mass pion angles, provided $|s|$, $|t|$, and $|u|$ are all large. Here $s = W^2$ is the squared invariant mass of the $\gamma^* p$ system and $u = (\gamma^* - N')^2$ is given in terms of the four-vectors $\gamma^* = e - e'$ and N' for the final-state nucleon. The large $|t|$ and $|u|$ region corresponds typically to a center-of-mass pion angle $\theta_{\text{cm}} \approx 90^\circ$. In particular, the CCR predict $d\sigma/dt = f(\theta_{\text{cm}}) s^{2-n}$ for the energy dependence of the cross section, where $f(\theta_{\text{cm}})$ depends on details of the dynamics of the process and n is the total number of point-like particles and gauge fields in the initial and final states. For example, our reaction $\gamma^* p \rightarrow n\pi^+$ should have $n = 9$, since there is one initial photon, three quarks in the initial and the final nucleons, and two in the final pion.

Open questions remain, including at which Q^2 and s do such scaling laws start to appear. Even if these respective scaling regimes are not reached at the present experimentally accessible Q^2 and s values, can one nevertheless extract GPDs or DAs, provided that some corrections to the QCD leading-twist mechanisms are applied? Only experimental data can help answer such questions.

II. INSIGHTS FROM PREVIOUS EXPERIMENTS

The two most recent experiments that have measured exclusive π^+ electroproduction off the proton, in the large- Q^2 , low- $|t|$ regime where the GPD formalism is potentially applicable, have been conducted in Hall C at Jefferson Lab (JLab) [5, 14, 15] and at HERMES [6].

The Hall C experiment, with 2 to 6 GeV electron beam energies, separated the σ_L and σ_T cross sections of the $\gamma^* p \rightarrow n\pi^+$ process using the Rosenbluth technique for $0.17 < x_B < 0.48$ and Q^2 up to 3.91 GeV^2 . The term σ_L dominated the cross section for $|t| < 0.2 \text{ GeV}^2$, while σ_T was dominant for larger $|t|$ values. These data were compared to two GPD-based calculations, hereafter referred to as VGG [16] and GK [11, 17] from the initials of the models' authors. For σ_L , which should be the QCD leading-twist contribution, these calculations were found to be in general agreement with the magnitude and the Q^2 - and t -dependencies of the experimental data. In these two calculations the main contribution to σ_L stems from the \tilde{E} GPD, which is modeled either entirely as pion-exchange in the t -channel [16] or is at least dominated by it [11, 17] (see Refs. [18, 19] for the connection between the t -channel pion-exchange and the \tilde{E} GPD). This term is also called the “pion pole”, and the difference between the two calculations lies in the particular choice made for the t -channel pion propagator (Reggeized or not) and the introduction of a hadronic form factor or not at the πNN vertex. In both calculations, σ_L contains higher-twist effects because the pure leading-twist com-

ponent of the pion pole largely underestimates the data. Only the GK model, which explicitly takes into account higher-twist quark transverse momentum, is able to reproduce σ_T . Agreement between data and calculation is found only if the H_T transversity GPD is introduced, which makes up most of σ_T .

The HERMES experiment used 27.6 GeV electron and positron beams to measure the $\gamma^*p \rightarrow n\pi^+$ cross section at four (x_B, Q^2) values, with x_B ranging from 0.08 to 0.35 and Q^2 from 1.5 to 5 GeV². No longitudinal/transverse separation was carried out. The differential cross section $d\sigma/dt$ was compared to the same two GPD models mentioned above. The GK model, which calculates both the longitudinal and transverse parts of the cross section, displays the same feature as for the lower energy JLab data, i.e. a dominance of σ_L up to $-t \approx 0.2$ GeV², after which σ_T takes over. The sum of the transverse and longitudinal parts of the cross section calculated by the GK model is in very good agreement with the data over most of the t range measured at HERMES [11, 17]. The VGG model, which calculates only the longitudinal part of the cross section, is in agreement with the data only for low t values [6]. Again, in both calculations, σ_L is dominated by the \tilde{E} GPD, modeled essentially by the pion pole term, and σ_T , in the GK model, is due to the transversity GPDs. The HERMES experiment also measured the transverse target spin asymmetry A_{UT} for the $\gamma^*p \rightarrow n\pi^+$ process, which indicate [11, 17] that the transversity GPDs H_T or \tilde{E}_T indeed play an important role in the process, confirming the approach of the GK group.

The comparison between the JLab Hall C and HERMES experiments and the two GPD-based calculations yields very encouraging signs that, although higher-twist contributions definitely play a major role, these data can be interpreted in terms of GPDs, in particular transversity GPDs. More precise and extensive data would be highly useful to confirm these findings. The present experiment covers 20 (x_B, Q^2) bins (with statistical errors of a few percent on average), which respectively doubles and triples the number of bins of the JLab Hall C and HERMES experiments. These new data are important to test the present GPD-based model calculations and, if successful, bring more stringent constraints on the current GPD parametrizations.

The large- $|t|$ (large- $|u|$) domain, where the DA formalism is asymptotically applicable for $\gamma^{(*)}p \rightarrow n\pi^+$, has so far been explored only in high-energy photoproduction at SLAC [1] and intermediate-energy photoproduction at JLab [20]. While the SLAC data tend to follow the s^{-7} scaling asymptotic prediction, for a 90° center-of-mass angle, the more recent JLab data, which are compatible with the SLAC data but are more precise, actually reveal some large oscillations around this s^{-7} behavior.

In recent years a similar trend, i.e. “global” scal-

ing behavior, has been observed in deuteron photodisintegration experiments [21–24], and also in hyperon photoproduction [25]. It would be interesting to see this in exclusive pion electroproduction and if so, whether the oscillations disappear as Q^2 increases. The measurement presented in this article is the first one to explore this large- $|t|$, large- $|u|$ domain ($\theta_{\text{cm}} \approx 90^\circ$) for $\sqrt{s} > 2$ GeV in π^+ exclusive electroproduction off the proton.

III. THE EXPERIMENT

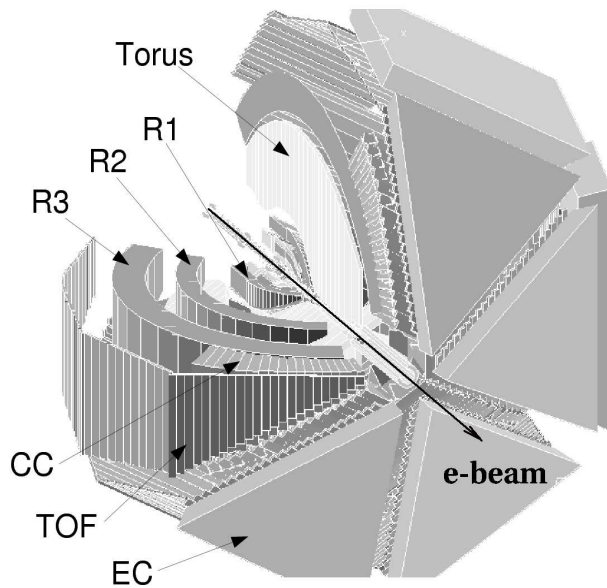


FIG. 2: Three-dimensional view of the CLAS detector.

The measurement was carried out with the CEBAF Large Acceptance Spectrometer (CLAS) [26]. A schematic view of CLAS is shown in Fig. 2. CLAS has a toroidal magnetic field generated by six flat superconducting coils (main torus), arranged symmetrically around the azimuth. Six identical sectors are independently instrumented with 34 layers of drift cells for particle tracking (R1, R2, R3), plastic scintillation counters for time-of-flight (TOF) measurements, gas threshold Cherenkov counters (CC) for electron and pion separation, and electromagnetic calorimeters (EC) for photon and neutron detection. To aid in electron/pion separation, the EC is segmented into an inner part closer to the target and an outer part further away from the target. CLAS covers on average 80% of the full 4π solid angle for the detection of charged particles. The azimuthal acceptance is maximum at a polar angle of 90° and decreases at forward angles. The polar angle coverage ranges from about 8° to 140° for the detection of π^+ . The scattered

electrons are detected in the CC and EC, which extend from 8° to 45° .

The target is surrounded by a small toroidal magnet (mini-torus). This magnet is used to shield the drift chambers closest to the target from the intense low-energy electron background resulting from Møller scattering.

The specific experimental data set “e1-6” used for this analysis was collected in 2001. The incident beam had an average intensity of 7 nA and an energy of 5.754 GeV. The 5-cm-long liquid-hydrogen target was located 4 cm upstream of the CLAS center. This offset of the target position was found to optimize the acceptance of forward-going positively charged particles. The main torus magnet was set at 90% of its maximum field. Empty-target runs were performed to measure contributions from the target cell windows.

In this analysis, the scattered electron and the produced π^+ were detected and the final state neutron determined from missing mass. The continuous electron beam provided by CEBAF is well suited for measurements involving two or more final-state particles in coincidence, leading to very small accidental coincidence contributions, smaller than 10^{-3} , for the instantaneous luminosity of $10^{34} \text{ cm}^{-2}\text{s}^{-1}$ of the present measurement.

Raw data were subjected to the calibration and reconstruction procedures that are part of the standard CLAS data analysis sequence. The reaction studied in this paper contributed only a fraction to the total event sample. Stringent kinematic cuts were applied to select events with one electron candidate and only one positively charged track. These events were then subjected to further selection criteria described in the following Section. All along the analysis, the experimental data distributions were compared to the output of our Monte Carlo code GSIM (see Section IV).

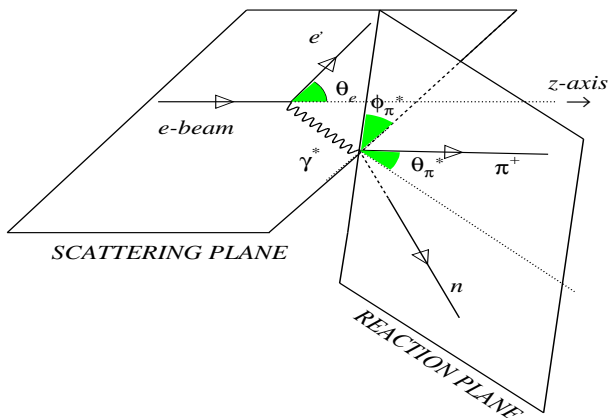


FIG. 3: Kinematics of exclusive single π^+ electroproduction from a proton target.

A schematic illustration of electron scattering off a nucleon target producing an outgoing nucleon and one pion is shown in Fig. 3. The scattered electron angle θ_e is given in the laboratory frame. The angle between the virtual photon three-momentum and the direction of the pion is denoted as θ_{π^*} and the angle between the electron scattering plane and hadronic production plane is denoted as ϕ_{π^*} . These two angles are defined in the center-of-mass frame of the hadronic system. The angle ϕ_{π^*} is defined so that the scattered electron lies in the $\phi_{\pi^*} = 0^\circ$ half plane with the z -axis pointing along the virtual photon momentum. For exclusive single π^+ production from the proton, the final state neutron is identified by the missing mass squared $((e + N) - (e' + p_{\pi}))^2$, where p_{π} is the four-momentum of the detected π^+ . The kinematic range and bin sizes are chosen to provide reasonable statistics in each bin. These are summarized in Table I.

TABLE I: Kinematic bins used in this analysis.

Variable	Number of bins	Range	Bin size
x_B	7	0.16 - 0.58	0.06
Q^2	5	1.6 - 3.1 GeV^2	0.3 GeV^2
	3	3.1 - 4.5 GeV^2	0.5 GeV^2
$-t$	6	0.1 - 1.9 GeV^2	0.3 GeV^2
	3	1.9 - 4.3 GeV^2	0.8 GeV^2
	1	4.3 - 5.3 GeV^2	1.0 GeV^2

IV. DATA ANALYSIS

A. Particle identification and event selection

1. Electron identification

The electrons are identified at the trigger level by requiring at least 640 MeV energy deposited in the EC in coincidence with a signal in the CC.

Additional requirements for particle identification (PID) were used in the off-line analysis to refine the electron identification. First, we required that the EC and CC hits matched with a reconstructed track in the drift chambers (DC). Second, we correlated the energy deposited in the EC and the momentum obtained by the track reconstruction in the DC. This is aimed at removing the pion contamination. Electrons deposit energy in proportion to their incident energy in the calorimeter whereas pions are minimum ionizing and deposit only a constant fraction of their energy in the calorimeter. The ratio of the total deposited energy in the EC to the momentum of the particle is called the sampling fraction. For electrons, approximately 30% of the total energy

deposited in the EC is directly measured in the active scintillator material. The remainder of the energy is deposited in the lead sheets interleaved between the scintillators. Figure 4 shows the sampling fraction E/p_e versus particle momentum p_e . The average sampling fraction for electrons was found to be 0.291 for this experiment. The solid lines in Fig. 4 show the $\pm 3\sigma$ sampling fraction cuts used in this analysis.

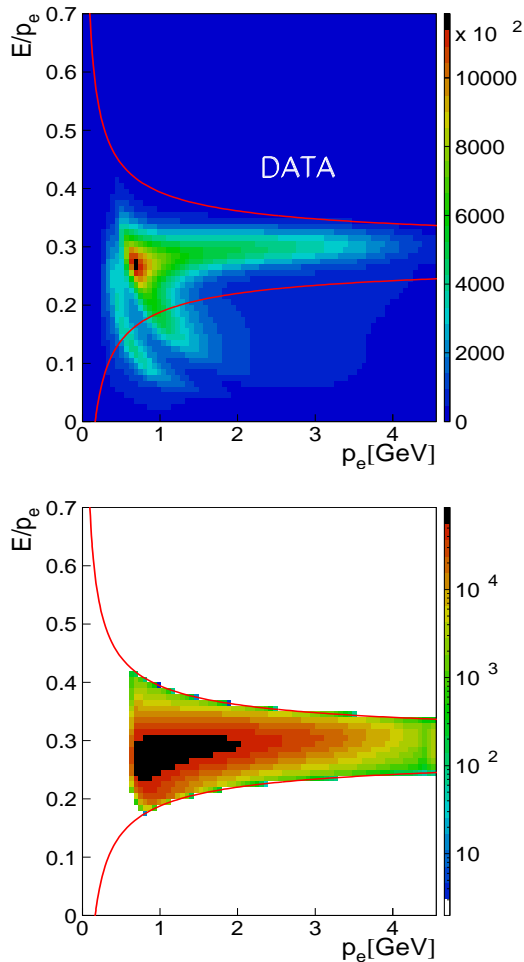


FIG. 4: (color online). EC sampling fraction versus particle momentum for the experimental data before (top) and after (bottom) EC energy cuts. The solid curves show the $\pm 3\sigma$ sampling fraction cuts which are applied to select electrons.

To further reject pions, we required the energy deposited in the inner EC to be larger than 50 MeV. Minimum ionizing particles lose less than this amount in the 15 cm thickness of the inner EC.

Fiducial cuts were applied to exclude the EC detector edges. When an electron hit is close to an edge, part of the shower leaks outside the device; in this case, the energy cannot be fully reconstructed from the calorime-

ter information alone. This problem can be avoided by selecting only those electrons lying inside a fiducial volume within the EC that excludes the edges. A GEANT-based simulation (GSIM) was used to determine the EC-response with full electron energy reconstruction. The calorimeter fiducial volume was defined by cuts that excluded the inefficient detector regions.

Particle tracks were reconstructed using the drift chamber information, and each event was extrapolated to the target center to obtain a vertex location. We demanded that the reconstructed z -vertex position (distance along the beam axis from the center of CLAS, with negative values indicating upstream of the CLAS center) lies in the range $-80 \text{ mm} < z_{\text{vtx}} < -8 \text{ mm}$.

Finally, a lower limit on the number of photoelectrons detected in the photomultiplier tubes of the CC provided an additional cut to improve electron identification. The number of photoelectrons detected in the CC follows a Poisson distribution modified for irregularities in light collection efficiency for the individual elements of the array. For this experiment, a good electron event was required to have 3 or more photoelectrons detected in the CC. The efficiency of the CC cut was determined from the experimental data. We fit the number of photoelectrons using the modified Poisson distribution. The efficiency range after the CC cut is 78% to 99% depending on the kinematic region. The correction is then the integral below the cut divided by the total integral of the resulting fit function.

2. Positively charged pion identification

The main cuts to select the π^+ are based on charge, z -vertex, fiducial cuts and velocity versus momentum correlations. The velocity β is calculated from the ratio of the path length of the reconstructed track, to the time of flight.

Figure 5 shows the β versus p distribution for positively charged particles from experimental data (top) and from the GSIM Monte Carlo simulation (bottom). A Gaussian is fit to β for bins in momentum p_π . A $\pm 1.5\sigma$ cut on β is chosen for pion candidates as shown in Fig. 5 (solid curves in the plot). Pions and positrons ($\beta = 1$) are well separated below $p_\pi = 250 \text{ MeV}/c$ of momentum in the experimental data, but this is no longer the case at momenta larger than $400 \text{ MeV}/c$. For this reason, positrons can be mis-identified as pions, which increases the background. At higher momenta, there can also be some particle mis-identification from protons and kaons. We estimated that the missing mass and vertex cuts reduce this mis-identification to the 5 - 10% level. This residual background contamination was subtracted as described in Sec. VI.

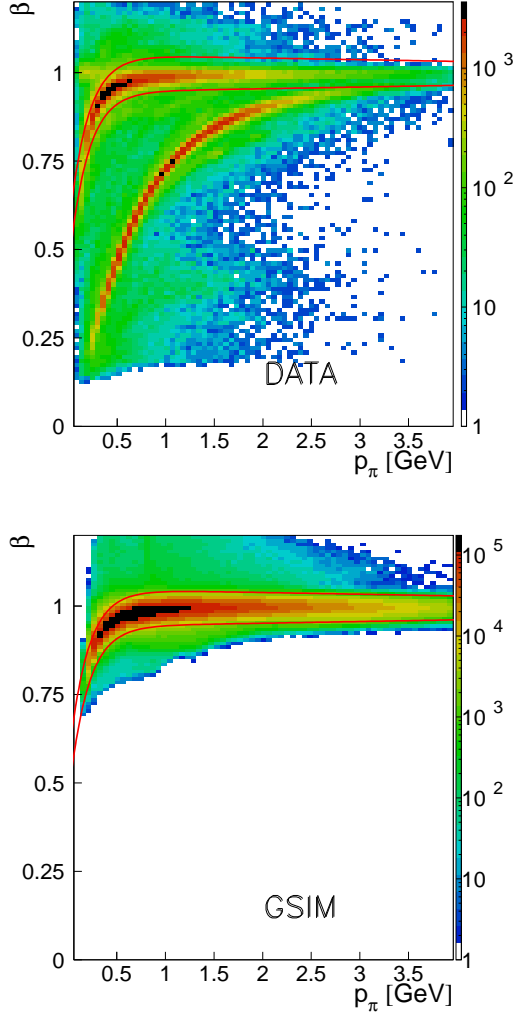


FIG. 5: (color online). Velocity β versus momentum for π^+ candidates using experimental data (top) and the GSIM Monte Carlo simulation (bottom). The solid curves are $\pm 1.5\sigma$ β cut lines used to select π^+ from positron ($\beta=1$ band) and proton ($\beta < 0.8$ band) backgrounds.

B. Fiducial cuts

1. Electron fiducial cuts

The fiducial cuts for electrons were developed to exclude regions with non-uniform detector efficiency such as the edges of a sector in the CC and EC. The fiducial cut is a function of the angles θ_e , ϕ_e , and momentum p_e of the electron. An example of such fiducial cut can be seen in Fig. 6 for a given electron momentum bin. In the bottom plots, one sees a central, uniform area, flanked by two fringes, separated by gaps. The solid line in the

top plot shows the boundary of the fiducial region for the central momentum in that bin. Only electron events inside the curve (blue area) were used in the analysis.

The criterion used to determine the electron fiducial region in terms of ϕ_e for a given momentum and θ_e bin is the detector efficiency. In order to eliminate the depletion region of the detector, we selected the flat high-efficient areas in the θ_e -sliced ϕ_e distributions. The histograms on the bottom of Fig. 6 show the ϕ_e distributions at two values of $\theta_e = 23^\circ \pm 0.5^\circ$ and $29^\circ \pm 0.5^\circ$. The highlighted area in the center indicates the selected fiducial range. In addition, a set of θ_e versus p_e cuts was used to eliminate the areas with a depleted number of events due to problematic time-of-flight counters, photomultiplier tubes in Cherenkov counters, or drift chamber areas.

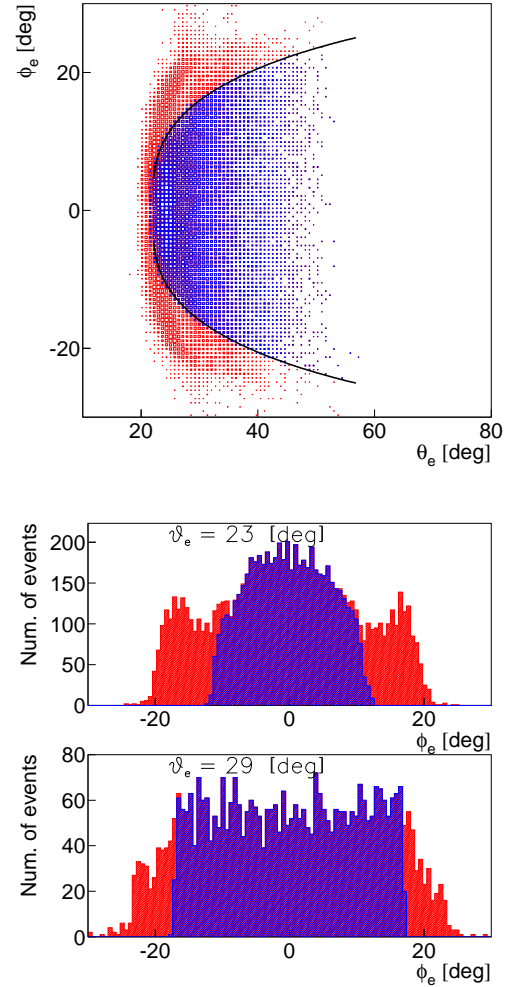


FIG. 6: (color online). Example of electron fiducial cuts for the electron momentum bin ($p_e = 1.437 \pm 0.025$ GeV) in Sector 2. See the detailed explanation in the text.

2. Pion fiducial cuts

The fiducial cuts for pions depend on the angles θ_π , ϕ_π and the momentum p_π . The pion momentum is scanned in 100 MeV steps from 0.3 to 1.7 GeV. The uniform detector efficiency region was determined by selecting a flat high-efficiency ϕ_π region in each θ_π -sliced momentum bin, and the bad TOF counters and the inefficient DC areas were excluded by additional software cuts (the same procedure as was applied to electrons). Figure 7 shows an example for the fiducial cuts for pions. The low-efficiency DC regions (between the black solid lines) and the bad TOF paddles (between red solid lines) are removed in both experimental (top) and simulated (bottom) data as part of the fiducial cuts.

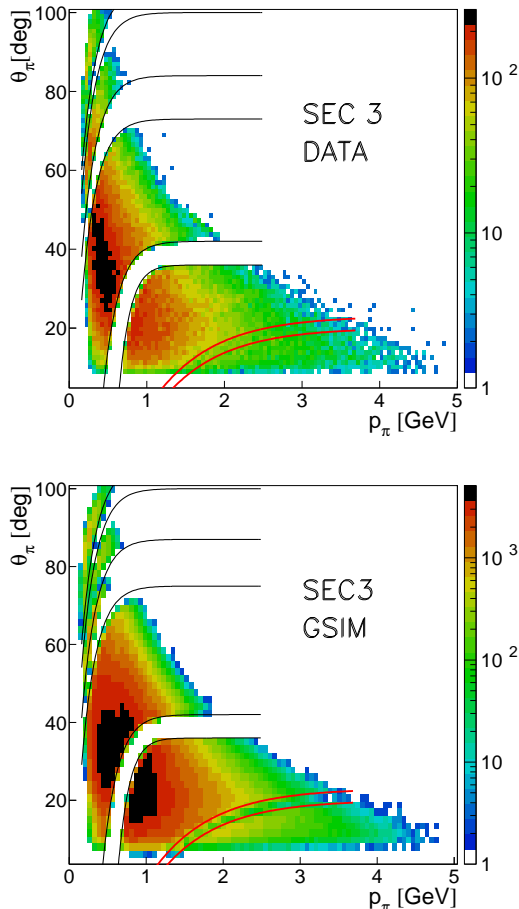


FIG. 7: (color online). Pion polar angular distribution as a function of momentum in Sector 3. The low detector response areas are removed by empirical cuts for experimental (top) and simulated data (bottom). The black thin solid curves are fiducial cuts based on DC inefficiencies and the red thick solid curves are cuts for bad TOF counters.

C. Kinematic corrections

Empirical corrections to the measured angles and momenta of both electrons and pions were applied to account for imperfect reconstruction due to drift chamber orientation and magnetic field uncertainties. A set of correction parameters was determined by minimizing the width and deviation of the missing mass peak position from the neutron mass. These corrections were as large as 5% of the pion momentum. They resulted in an improved missing mass resolution, from 35 to 23 MeV on average depending on kinematics. The corrections were most sizable for the high-momentum and forward-angle pions at high W which are of interest in this experiment.

V. MONTE CARLO SIMULATION

In order to calculate the CLAS acceptance for $ep \rightarrow e'\pi^+n$, we simulated electron and pion tracks using the CLAS GEANT3-based Monte Carlo Package GSIM. For systematic checks, we used two Monte Carlo event generators. The first, GENEV [28], generates events for various exclusive meson electroproduction reactions for proton and neutron targets (π , ω , ρ^0 , and ϕ), including their decay, radiative effects, and resonant and non-resonant multi-pion production, with realistic kinematic distributions. GENEV uses cross section tables based on existing photoproduction data and extrapolates to electroproduction by introducing a virtual photon flux factor (Γ) and the electromagnetic form factors. Radiative effects, based on the Mo and Tsai formula [29], are part of this event generator as an option. Although the formula is exact only for elastic e - p scattering, it can be used as a first approximation to simulate the radiative tail and to estimate bin migration effects in our pion production process, as will be discussed in Sec. VB. The second event generator, FSGEN [30], distributes events according to the $ep \rightarrow e'\pi^+n$ phase space.

Electrons and positive pions were generated under the “e1-6” experimental conditions. Events were processed through GSIM. We then applied additional ad-hoc smearing factors for the tracking and timing resolutions so that they matched the experimental data. The low-efficiency regions in the drift chambers and problematic TOF channels were removed during this procedure. Acceptance and radiative corrections were calculated for the same kinematic bins as were used for the yield extraction as shown in Table I. Figure 8 shows the binning in Q^2 and x_B applied in this analysis. The cross sections were then calculated from the yields in each bin, taking into account acceptance and radiative corrections as described below, as well as bin size corrections.

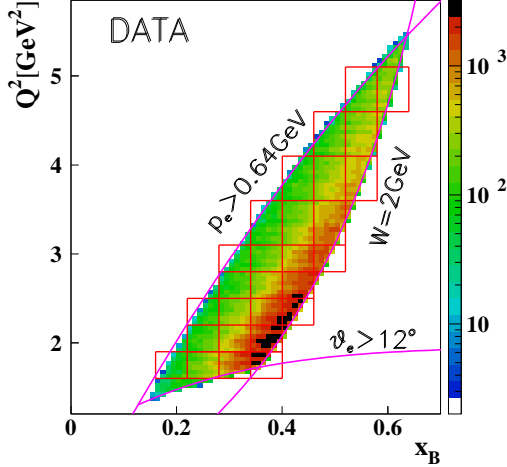


FIG. 8: (color online). Kinematic coverage and binning (red boxes) as a function of x_B and Q^2 (integrated over all other variables) for the experimental data. Only events with $W > 2$ GeV are shown.

A. Acceptance corrections

We related the experimental yields to the cross sections using the acceptance, including the efficiency of the detector. The acceptance factor (Acc) compensates for various effects, such as the geometric coverage of the detector, hardware and software inefficiencies, and resolution from track reconstruction. We generated approximately 850 million events, taking radiative effects into account. This results in a statistical uncertainty for the acceptance determination of less than 5% for most bins.

We define the acceptance as a function of the kinematic variables,

$$Acc(x_B, Q^2, -t, \phi_\pi^*) = \frac{N^{REC}(x_B, Q^2, -t, \phi_\pi^*)}{N^{GEN}(x_B, Q^2, -t, \phi_\pi^*)}, \quad (1)$$

where N^{REC} is the number of reconstructed particles and N^{GEN} is the number of generated particles in each kinematic bin. The acceptances are between 1 and 9%. Figure 9 shows examples of acceptances, determined with the GENEV+GSIM packages, as a function of the angle ϕ_π^* at a given Q^2 for various x_B and t bins.

B. Radiative correction

We calculated the radiative correction in the region $W > 2$ GeV using the complete simulation GENEV plus GSIM to take into account the effects of the radiation of real photons. These real Bremsstrahlung photons can

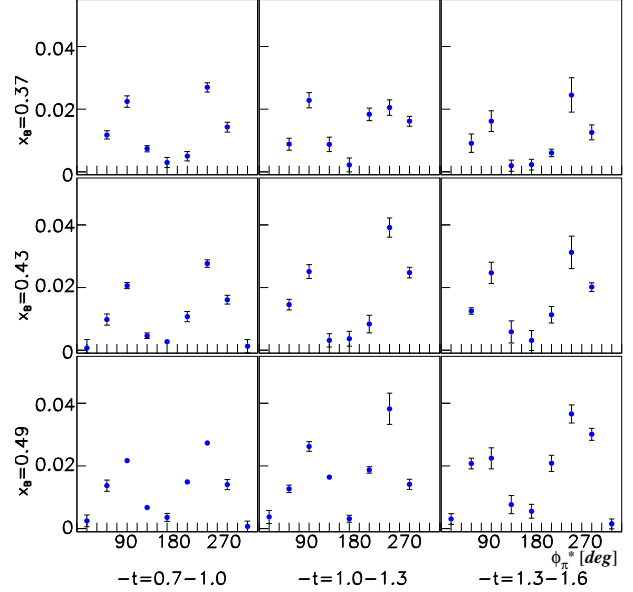


FIG. 9: (color online). Examples of acceptance as a function of ϕ_π^* for various t and x_B bins at $Q^2 = 2.35$ GeV². The dips at $\phi_\pi^* = 0^\circ$ and 180° are due to sector boundaries in CLAS.

originate either from the primary hard scattering at the level of the target proton (internal radiation) or, from the interaction of the scattered or the initial electron with the various material layers of the CLAS detector that it crosses (external radiation). The GENEV code allows us to calculate of the new value of the incoming electron energy before the reaction takes place. The effects of the radiation of hard photons (for instance, the loss of events due to the application of a cut on the neutron missing mass) are already taken into account by the Monte Carlo acceptance calculation described in the previous section. Figure 10 shows examples of the simulated neutron missing mass with and without radiative effects in two W bins, obtained with the GENEV event generator and GSIM. Again, the Monte Carlo simulations were carried out with the same cut procedures and conditions as used in the data analysis.

The correction due to soft photons and virtual corrections are determined by extracting the ratio between the number of events without radiative and with radiative effects at the level of the event generator. This radiative-correction factor is calculated for each kinematic bin used in the data analysis.

As a check, the radiative-correction factors were also calculated with the EXCLURAD code [31], which contains a complete description of all internal radiative effects in exclusive processes, but is currently valid only up to $W = 2$ GeV. We compare the two different

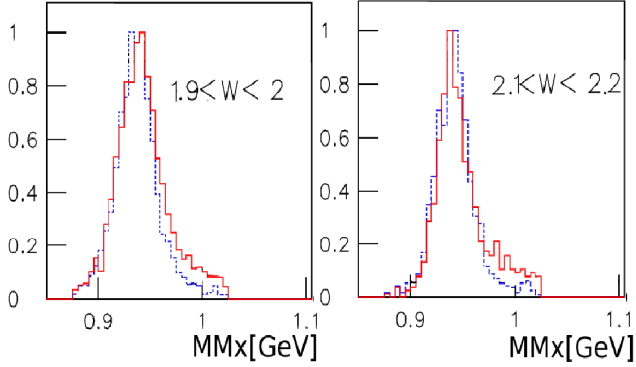


FIG. 10: (color online). The simulated neutron missing mass distributions for two W bins with $\Delta W = 100$ MeV at $W = 1.95$ (left) and 2.15 (right) GeV integrated over ϕ_π^* , $\cos\theta_\pi^*$, and Q^2 . Normalized yields are shown with (solid red) and without (dashed blue) radiative effects.

radiative-correction methods in a kinematic region where both methods are valid. Figure 11 shows the results for radiative-correction factors in the region $W \approx 1.75$ GeV and $Q^2 \approx 3$ GeV² as a function of $\cos\theta_\pi^*$.

The radiative correction factors from EXCLURAD are within $\pm 20\%$ of unity over the full $\cos\theta_\pi^*$ range (red solid points). The radiative corrections from GENEV+GSIM also fluctuate around 1.0 with a similar structure (blue open circles). The error bars are due to Monte Carlo statistics. The agreement between the two approaches is important because EXCLURAD is believed to be the most reliable of the two methods because it does not have the limitations of Mo and Tsai. Building on this reasonable agreement in this part of the phase space, we rely on the GENEV+GSIM radiative-correction factors for our data. In Sec. VII, we discuss the systematic uncertainty associated with these radiative corrections.

VI. BACKGROUND SUBTRACTION

There are two main sources of background in our reaction. One consists of the mis-identification of pions with other positively charged particles (protons, kaons, positrons). This is particularly important for the pion-proton separation at high-momenta ($p > 2$ GeV), see Sec. IV A. The other consists of multi-pion production. To subtract both backgrounds, we fit the neutron missing mass distribution bin by bin. The background was fit to an exponential plus a Gaussian. The former function was determined from simulations of the multi-pion spectra in the neutron missing mass region > 1.02 GeV. Figure 12 (top) shows an example of such a background

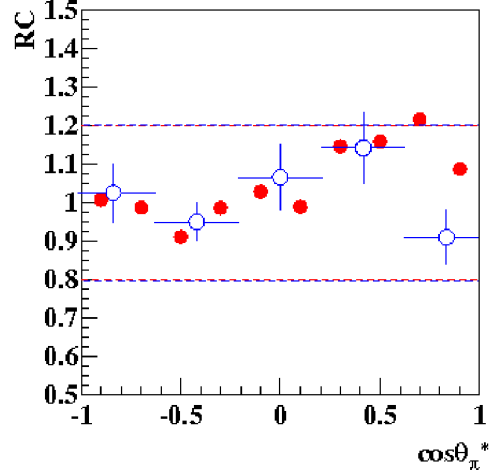


FIG. 11: (color online). Radiative-correction factors (RC) as a function of $\cos\theta_\pi^*$ from EXCLURAD (red solid points) at $W = 1.74$ GeV, $Q^2 = 3$ GeV², and $\phi_\pi^* = 112.5^\circ$ and GENEV plus GSIM (blue open circle) at $W \approx 1.75$ GeV, $Q^2 \approx 3$ GeV², and $80^\circ < \phi_\pi^* < 120^\circ$.

fit. A comparison of the missing mass (MMx) spectrum is shown in the bottom plot of Fig. 12 before (black squares) and after (red solid circles) background subtraction. In the range of the neutron missing mass cut, shown by the two vertical lines at 0.877 GeV and 1.0245 GeV, the background is small, and the remaining radiative tail becomes visible after the background is subtracted.

VII. SYSTEMATIC UNCERTAINTIES

Several sources of systematic uncertainty that can affect our measurements have been studied by changing various cuts and using different event generators.

We varied the criteria used for the particle identification to provide more and less stringent particle selection and reran the complete analysis. The cuts on EC energy deposition and CC amplitude for the electron, as well as cuts on the TOF timing for the pion, have been varied. The EC sampling fraction cut was varied from $\pm 3\sigma_{EC}$ to $\pm 2\sigma_{EC}$ which led to a 5% uncertainty for electron identification. Changing the TOF β cut from $\pm 2\sigma_{TOF}$ to $\pm 2.5\sigma_{TOF}$ for pion identification gives a 1.7% uncertainty. The various cuts for channel identification such as fiducial, missing mass, and vertex cuts produced 3%, 1%, and 1.6% systematic uncertainties, respectively.

Acceptance and radiative corrections are the biggest sources of systematic errors. The systematic uncertainty from the acceptance is evaluated by comparing our results using the GENEV and FSGEN event generators. In the

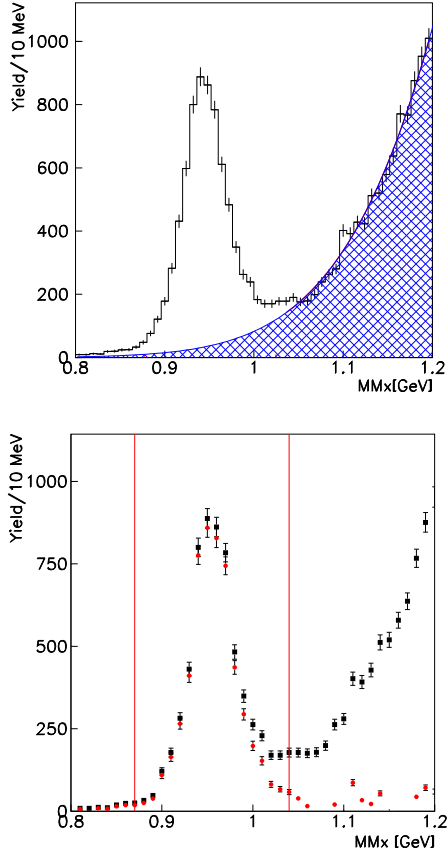


FIG. 12: (color online). Example of the missing mass peak plus background at $Q^2 = 2.65 \text{ GeV}^2$, $-t = 1.15 \text{ GeV}^2$, and $x_B = 0.43$. The top plot shows the fitted background distribution (hashed region). The bottom plot shows the neutron missing mass distribution before (black squares) and after (red solid points) background subtraction.

limit of infinitely large statistics and infinitely small bin size, our acceptances should be model-independent (up to the bin-migration effects). But these conditions are not reached here and we find differences between 2 and 8%. The systematic uncertainty for radiative corrections is estimated similarly by comparing the radiative-correction factors (GENEV and EXCLURAD). We calculated the difference between the cross sections corrected for radiative effects using either GENEV-GEANT simulation or the W -expanded EXCLURAD (where EXCLURAD was linearly extrapolated to $W > 2 \text{ GeV}$). An average 8% systematic uncertainty was found. Acceptance and radiative corrections are actually correlated, but after a combined analysis we estimated an average 9.5% total uncertainty for both of these effects together.

Concerning the background subtraction procedure un-

der the neutron missing mass (see Sec. VI), we used various fitting functions (Gaussian plus exponential, Gaussian plus polynomial, exponential plus polynomial, etc.) and various fitting ranges. These various fitting functions and ranges eventually produced small differences and we estimated a 3% systematic uncertainty associated with this procedure.

These latter systematic uncertainties were determined for each bin. Concerning overall scale uncertainties, the target length and density have a 1% systematic uncertainty and the integrated charge uncertainty is estimated at 2%. The total systematic uncertainties, averaged over all bins, is then approximately 12%. Table II summarizes the systematic uncertainties in this analysis averaged over all the accessible kinematic bins seen in Fig. 8.

TABLE II: Average systematic uncertainties for the differential cross sections.

Source	Criterion	Estimated contribution
e^- PID	sampling fraction cut in EC ($3\sigma_{\text{SF}} \rightarrow 2\sigma_{\text{SF}}$)	5%
e^- fiducial cut	fiducial volume change (10% reduced)	2.5%
π^+ PID	β resolution change ($2\sigma_{\text{TOF}} \rightarrow 2.5\sigma_{\text{TOF}}$)	1.7%
π^+ fiducial cut	width (10% reduced)	3.5%
Missing mass cut	neutron missing mass resolution ($3\sigma_{\text{MMx}} \rightarrow 3.5\sigma_{\text{MMx}}$)	1%
Vertex cut	z -vertex width (5% reduced)	1.6%
Acceptance	GENEV versus FSGEN	
Radiative corrections	GENEV versus EXCLURAD	9.5%
LH2 target	density/length	1%
Luminosity	integrated charge	2%
Background subtraction	various fit functions exponential, gaussian and high order polynomials	3%
Total		12%

VIII. RESULTS AND DISCUSSION

In this section, we present our results for the cross sections of the $p(e, e'\pi^+)n$ reaction in the invariant mass region $W > 2$ GeV. We have extracted the differential cross sections as a function of several variables (t , Q^2 , and W or x_B). The angle ϕ_π^* is always integrated over in the following. The error bars on all cross sections include both statistical and systematic uncertainties added in quadrature.

A. $d\sigma/dt$ as a function of t

Fig. 13 shows the differential cross section $d\sigma/dt$ as a function of t for different (x_B, Q^2) bins. We define the reduced differential cross section:

$$\frac{d\sigma}{dt} = \frac{1}{\Gamma} \frac{d^3\sigma}{dQ^2 dx_B dt}, \quad (2)$$

where the virtual photon flux factor [32] has been factored out.

We have included in Fig. 13 the JLab Hall C data, which cover only the very small t domain. The JLab Hall C data central (t , Q^2 , and W or x_B) values do not exactly match our central (t , Q^2 , and W or x_B) kinematics but are sufficiently close to allow for a reasonable comparison.

We note that there is generally good agreement between the results of the two experiments. For better visualization, which is also relevant for the comparison with the models, we also show Fig. 14 which concentrates on the low $|t|$ range of Fig. 13.

The $d\sigma/dt$ cross sections fall exponentially as $|t|$ increases, with some flattening at large $|t|$, which is a feature that is also observed in photoproduction [1, 20]. For several bins, for instance $(x_B, Q^2)=(0.31, 1.75)$ or $(0.37, 2.05)$, we notice a structure in $d\sigma/dt$ for $|t| \approx 0.5$ GeV². The origin of this dip is not known. The JLab Hall C experiment [15] also measured such a structure in $d\sigma/dt$ (see Fig. 13 in Ref. [15] for bin $(W, Q^2)=(1.8, 2.16)$).

We first compare our data to a calculation using hadronic degrees of freedom. This is the Laget model [33] based on Reggeized π^+ and ρ^+ meson exchanges in the t -channel [34]. The hadronic coupling constants entering the calculation are all well-known or well-constrained, and the main free parameters are the mass scales of the electromagnetic form factors at the photon-meson vertices.

If one considers only standard, monopole, Q^2 -dependent form factors, one obtains much steeper t -slopes than the data. An agreement with the data can be recovered by introducing a form factor mass scale that also depends on t according to the prescription of Ref. [33]. This

form factor accounts phenomenologically for the shrinking in size of the nucleon system as t increases. The size of the effect is quantitatively the same as in the $p(e, e'\omega)p$ channel (see Fig. 1 of Ref. [33]), which is dominated by pion exchange in the same energy domain as in our study. The results of this calculation with (Q^2, t) -dependent meson electromagnetic form factors are shown, for $d\sigma_T/dt$, $d\sigma_L/dt$, and $d\sigma/dt = d\sigma_T/dt + \epsilon d\sigma_L/dt$, in Figs. 13 and 14 by the red curves. The Laget model gives a qualitative description of the data, with respect to the overall normalization at low t and the x_B -, Q^2 - and t -dependences. We recall that this model already gives a good description of the photoproduction data (SLAC, JLab) and of the HERMES electroproduction data, and that the form factor mass scale [33] has not been adjusted to fit our data.

In the framework of this model, $d\sigma_L/dt$ dominates at low $|t|$, while $d\sigma_T/dt$ takes over around $|t| \approx 0.5$ GeV², this value being approximately the same for all (Q^2, x_B) bins. This dominance of σ_L at low $|t|$ is a consequence of the t -channel π^+ -exchange (pion pole). At larger $|t|$, the ρ^+ meson exchange, which contributes mostly to the transverse part of the cross section, begins to dominate. The Laget Regge model, in addition to t -channel meson exchanges, also contains u -channel baryon exchanges. It thus exhibits an increase of the cross section in some (Q^2, x_B) bins at the largest $|t|$ -values, corresponding to low- $|u|$ values. We have additional data at larger $|t|$ (lower $|u|$) that are currently under analysis.

We now turn to the partonic approach of the GK model, which is based on the handbag GPD formalism. In this model $d\sigma_L/dt$ is mostly generated by the pion pole, similar to the Laget Regge model. There are, however, a couple of important differences in the treatment of this pion pole in the two calculations. The Laget model has an intrinsic energy dependence. It is “Reggeized”, so the t -channel propagator is proportional to $s^{\alpha_\pi(t)}$, where $\alpha_\pi(t)$ is the pion Regge trajectory. In addition, it uses a (Q^2, t) -dependent electromagnetic form factor. These two features change the s -, x_B -, and t -dependences of the pion pole with respect to the GK treatment. Indeed, in the latter case, the t -channel pion propagator is proportional to $1/(t - m_\pi^2)$, so it has no s -dependence, and the hadronic form factor at the πNN vertex is only t -dependent.

Figures 13 and 14 also show the results of the GK calculation (in blue) for $d\sigma_L/dt$ and $d\sigma/dt$. We see that $d\sigma_L/dt$ has a non-negligible contribution only in the low $|t|$ domain and only for a few (x_B, Q^2) bins, in particular at the lowest x_B and the largest Q^2 values. This is in line with the observation that at HERMES kinematics, i.e. at lower x_B and larger Q^2 values, the longitudinal part of the cross section dominates in the GK model at low $|t|$. For the larger (Q^2, x_B) phase space in the present experiment, one sees that the dominance of $d\sigma_L/dt$ at low $|t|$

is not at all systematic in the GK calculation. The ratio of $d\sigma_L/dt$ to $d\sigma/dt$ strongly depends on x_B . Specifically, it decreases as x_B increases and at $x_B=0.49$, $d\sigma_L/dt$ is only a few percent of $d\sigma/dt$, even at the lowest t values. This is a notable difference from the Laget Regge model.

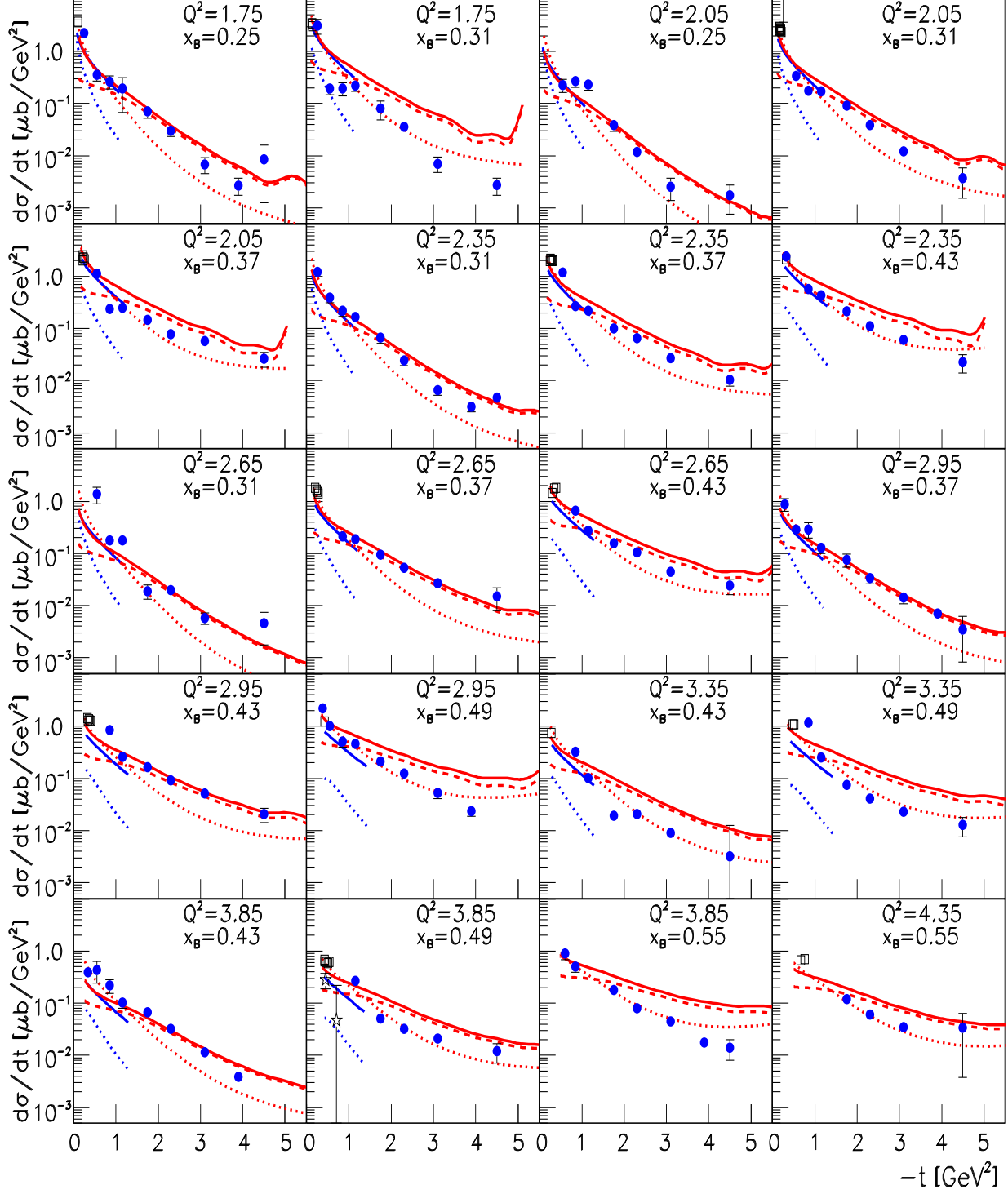


FIG. 13: (color online). Differential cross sections $d\sigma/dt$ [μb/GeV²] integrated over ϕ_π^* for various (Q^2, x_B) bins. The blue solid points are the present work. The black open squares ($d\sigma/dt$) [15] and open stars ($d\sigma_L/dt$) [5] are the JLab Hall C data. The red solid ($d\sigma/dt$), dotted ($d\sigma_L/dt$), and dashed ($d\sigma_T/dt$) curves are the calculations from the Laget model [33] with (Q^2, t) -dependent form factors at the photon-meson vertex. The blue solid and dotted lines are $d\sigma/dt$ and $d\sigma_L/dt$, respectively, from the GK model [17].

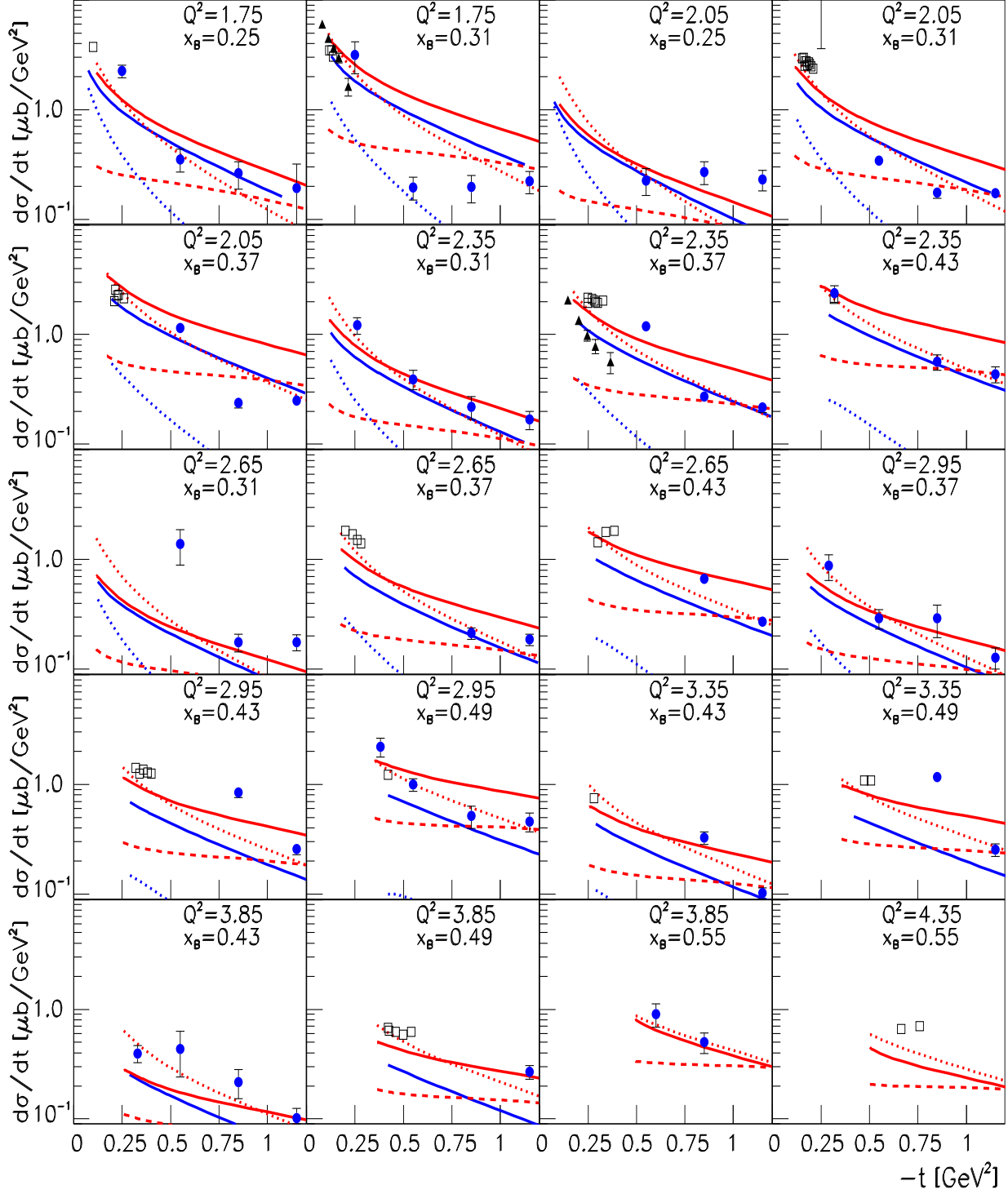


FIG. 14: (color online). Same as Fig. 13 except with an expanded low $|t|$ scale. In addition, the black solid triangles [14] show the JLab Hall C extracted $d\sigma_L/dt$ data.

In the GK model, the transverse part of the cross section is due to transversity GPDs. It describes qualitatively our low- t data over our whole (x_B, Q^2) domain. This is remarkable since the GK model was optimized for higher-energy kinematics (HERMES) and no further adjustments were made for the present CLAS kinematics. The GK model is applicable only for small values of $-t/Q^2$. Outside this regime, higher-twist contributions that are not taken into account in the GK handbag formalism are expected. In Fig. 13, the GK calculation predicts that the transverse part of the cross section dominates essentially everywhere in our kinematic domain. This means that, if the GK L/T ratio and model-dependent treatment of higher-twist corrections are correct, then the exclusive π^+ electroproduction process provides an original and exciting way to access transversity GPDs. This obviously indicates the need of new L/T separated cross sections at large x_B , which will become available with the upcoming JLab 12-GeV upgrade.

B. $d\sigma/dt$ as a function of Q^2 at fixed t

Figure 15 shows the differential cross section $d\sigma/dt$ as a function of Q^2 at fixed x_B for various t values. As seen in Fig. 13, both the Laget and GK model calculations provide a decent description of the magnitude and Q^2 -dependence of $d\sigma/dt$. The Laget model seems to have a slightly steeper Q^2 -dependence than the GK model. In any case, the limited precision and lever arm of our data don't allow favoring one model over the other. Because of the relatively low Q^2 range accessed in this experiment, higher-twist effects are expected to contribute and hence the leading-twist $1/Q^6$ dependence of σ_L is no longer expected. We fit our data with a $1/(Q^2)^n$ dependence. The resulting exponents n indeed indicate a flatter Q^2 dependence than $1/Q^6$. This again should be investigated at higher Q^2 together with the above-mentioned L/T separation.

C. $d\sigma/dt$ as a function of W at fixed θ_π^*

Figure 16 shows our scaled cross sections, $s^7 d\sigma/dt$, as a function of W for four Q^2 values and for four bins in $\cos\theta_\pi^*$: -0.01 ± 0.16 , 0.27 ± 0.1 , 0.42 ± 0.05 and 0.53 ± 0.06 . The lever arm in W is limited. At $\theta_\pi^* = 90^\circ$, where the scaling behavior is expected to set in most quickly, we have only 2 or 3 data points in W , depending on the Q^2 bin. It is therefore difficult to draw precise conclusions at this stage for the W -dependence at fixed Q^2 . Nevertheless, with these limited (but unique) data, one can say that, at $\theta_\pi^* = 90^\circ$, except for the 3 data points at $Q^2 = 2.35$ GeV², the W -dependence of $s^7 d\sigma/dt$ does not appear to be constant. We also display in Fig. 16 the result of the

Laget model. It gives, within a factor two, a general description of these large-angle data. The W -dependence is very similar to the energy dependence that was observed in photoproduction [2]. In the same energy range as covered by the present study, real photon data exhibit strong deviations from scaling. Within the Laget model, these deviations are well accounted for by the coupling between the $n\pi^+$ and the ρN channels [35]. The JLab 12-GeV upgrade will allow us to increase the coverage in W and check whether this finding remains valid in the virtual photon sector.

IX. SUMMARY

In summary, we have measured the cross sections of exclusive electroproduction of π^+ mesons from protons as a function of $-t = 0.1 - 5.3$ GeV², $x_B = 0.16 - 0.58$, and $Q^2 = 1.6 - 4.5$ GeV². We have compared our differential cross sections to two recent calculations based on hadronic degrees of freedom (Laget Regge) and on partonic degrees of freedom (GK handbag). Both models give a qualitative description of the overall strength and of the t -, Q^2 - and x_B -dependencies of the data. To achieve this, the Regge model needs (Q^2, t) -dependent electromagnetic form factors while the handbag model needs transversity GPDs. The two approaches differ in the relative contributions of the longitudinal and transverse parts of the cross section, in particular as x_B increases. Experimentally, L-T separated cross sections, which can be extracted with the upcoming 12-GeV upgrade, are needed to distinguish between the two approaches. If the handbag approach is confirmed, the $p(e, e'\pi^+)n$ process offers the outstanding potential to access transversity GPDs.

X. ACKNOWLEDGMENT

We acknowledge the outstanding efforts of the staff of the Accelerator and the Physics Divisions at Jefferson Lab that made this experiment possible. We also give many thanks to P. Kroll and S. Goloskokov for their calculation. The early work of D. Doré on this analysis is also acknowledged. This work was supported in part by the US Department of Energy, the National Science Foundation, the Italian Istituto Nazionale di Fisica Nucleare, the French Centre National de la Recherche Scientifique, the French Commissariat à l'Energie Atomique, the United Kingdom's Science and Technology Facilities Council, the Chilean Comisión Nacional de Investigación Científica y Tecnológica (CONICYT), and the National Research Foundation of Korea. The Southeastern Universities Research Association (SURA) operated

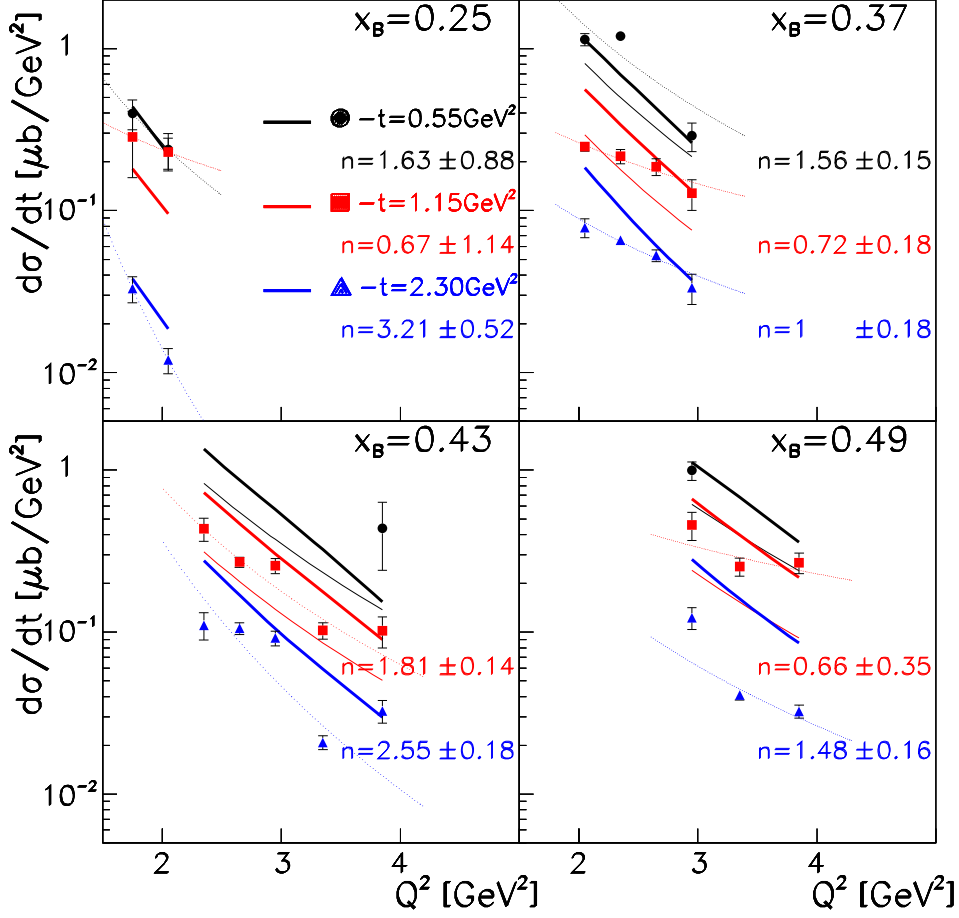


FIG. 15: (color online). Differential cross sections $d\sigma/dt$ [$\mu\text{b}/\text{GeV}^2$] versus Q^2 at fixed x_B for various t values. The dotted curves are the results of a fit to the function $A/(Q^2)^n$. The bold solid curves are the Laget calculations [33] and the thin solid curves are the GK calculations [17]. The GK calculation are only valid for $-t < \approx 1$ GeV^2 so we do not display those results for $-t = 2.3$ GeV^2 . When only one solid curve is visible, the Laget and GK calculations overlap.

the Thomas Jefferson National Accelerator Facility for
the US Department of Energy under Contract No.DE-

AC05-84ER40150.

-
- [1] R. L. Anderson *et al.*, Phys. Rev. D **14**, 679 (1976); C. White *et al.*, Phys. Rev. D **49**, 58 (1994).
 - [2] W. Chen *et al.*, Phys. Rev. Lett. **103**, 012301 (2009).
 - [3] C. J. Bebek *et al.*, Phys. Rev. D **13**, 25 (1976).
 - [4] C. J. Bebek *et al.*, Phys. Rev. D **13**, 1693 (1978).
 - [5] T. Horn *et al.*, Phys. Rev. C **78**, 058201 (2008).
 - [6] A. Airapetian *et al.*, Phys. Lett. B **659**, 486 (2008).
 - [7] D. Müller, D. Robaschik, B. Geyer, F.-M. Dittes, and J. Horejsi, Fortschr. Phys. **42**, 101 (1994).
 - [8] X. Ji, Phys. Rev. Lett. **78**, 610 (1997); Phys. Rev. D **55**, 7114 (1997).
 - [9] A.V. Radyushkin, Phys. Lett. B **380** (1996) 417; Phys. Rev. D **56**, 5524 (1997).
 - [10] J. C. Collins, L. Frankfurt, and M. Strikman, Phys. Rev. D **56**, 2982 (1997).
 - [11] S. V. Goloskokov and P. Kroll, Eur. Phys. J. C **65**, 137 (2010).
 - [12] S. J. Brodsky and G. P. Lepage, Phys. Rev. D **22**, 2157 (1980).
 - [13] S. J. Brodsky and G. R. Farrar, Phys. Rev. Lett. **31**, 1153 (1973); Phys. Rev. D **11**, 1309 (1975); V. Matveev *et al.*, Nuovo Cimento Lett. **7**, 719 (1973).
 - [14] H. P. Blok *et al.*, Phys. Rev. C **78**, 045202 (2008).
 - [15] X. Qian *et al.*, Phys. Rev. C **81**, 055209 (2010).

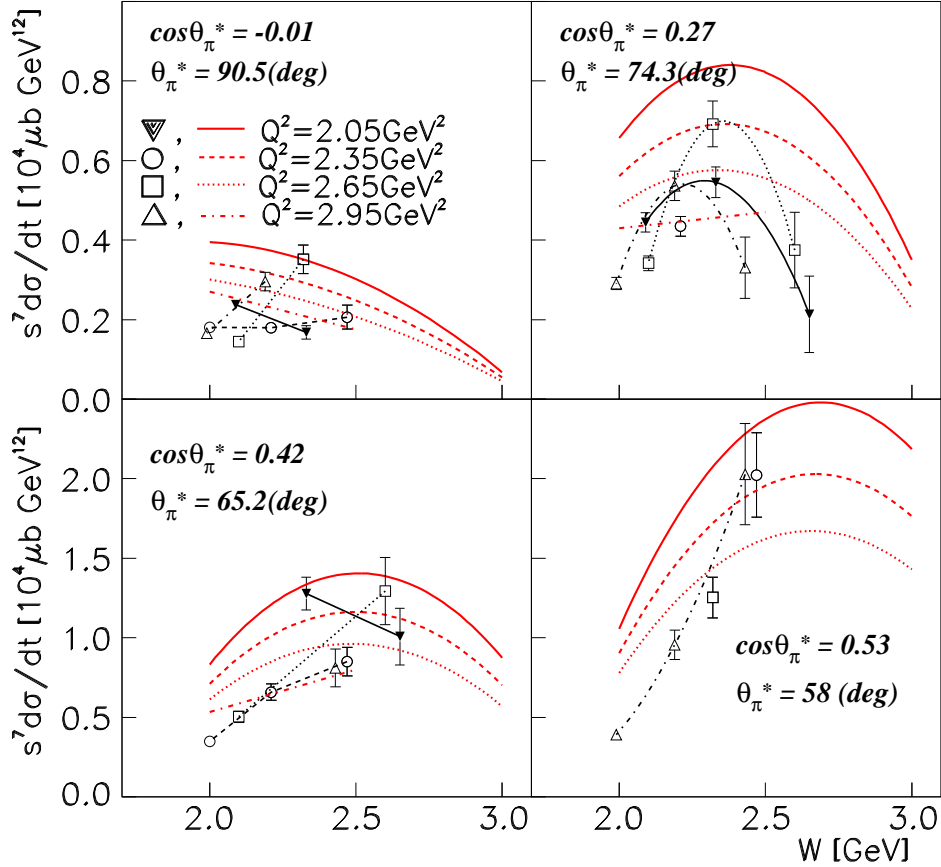


FIG. 16: (color online). Scaled cross sections $s^7 d\sigma/dt$ [$10^4 \mu\text{b GeV}^{12}$] versus W for $\theta_\pi^* = 60^\circ$ to 90° and various Q^2 bins. Red curves are from the Laget model [33]. The black curves are to guide the eye, connecting points with the same Q^2 values.

- [16] M. Vanderhaeghen, P. A. M. Guichon, and M. Guidal, Phys. Rev. D **60**, 094017 (1999).
- [17] S. V. Goloskokov and P. Kroll, Eur. Phys. J. A **47**, 112 (2011).
- [18] L. Mankiewicz, G. Piller and A. Radyushkin, Eur. Phys. J. C **10**, 307 (1999).
- [19] L. Frankfurt, P. Pobylitsa, M. Poliakov, and M. Strikman, Phys. Rev. D **60**, 014010 (1999).
- [20] L. Y. Zhu *et al.*, Phys. Rev. Lett. **91**, 022003 (2003), Phys. Rev. C **71**, 044603 (2005).
- [21] J. Napolitano *et al.*, Phys. Rev. Lett. **61**, 2530 (1988); S. J. Freedman *et al.*, Phys. Rev. C **48**, 1864 (1993); J. E. Belz *et al.*, Phys. Rev. Lett. **74**, 646 (1995).
- [22] C. Bochna *et al.*, Phys. Rev. Lett. **81**, 4576 (1998).
- [23] E. C. Schulte *et al.*, Phys. Rev. Lett. **87**, 102302 (2001).
- [24] P. Rossi *et al.*, Phys. Rev. Lett. **94**, 012301 (2005); M. Mirazita *et al.*, Phys. Rev. C **70**, 014005 (2004).
- [25] R. A. Schumacher and M. M. Sargsian, Phys. Rev. C **83**, 025207 (2011).
- [26] B.A. Mecking *et al.*, Nucl. Instrum. Methods A **51**, 409 (1995).
- [27] K. Park *et al.*, Phys. Rev. C **77**, 015208 (2008).
- [28] E. Golovach, M. Ripani, M. Battaglieri, R. De Vita, private communication.
- [29] L. W. Mo, Y. S. Tsai, Rev. Mod. Phys. **41**, 205 (1969).
- [30] S. Stepanyan, private communication.
- [31] A. Afanasev *et al.*, Phys. Rev. D **66**, 074004 (2002).
- [32] L. Hand, Phys. Rev. **129**, 1834 (1963).
- [33] J. M. Laget, Phys. Rev. D **70**, 054023 (2004).
- [34] M. Guidal, J. M. Laget and M. Vanderhaeghen, Nucl. Phys. A **627**, 645 (1997), Phys. Lett. B **400**, 6 (1997).
- [35] J. M. Laget, Phys. Lett. B **685**, 146 (2010).